Remote Sensing of Environment 260 (2021) 112439

Contents lists available at ScienceDirect

Remote Sensing of Environment

journal homepage: www.elsevier.com/locate/rse

Cross-calibration of MODIS and VIIRS long near infrared bands for ocean color science and applications

Brian B. Barnes [a,*], Chuanmin Hu [a], Sean W. Bailey [b], Nima Pahlevan [b,c], Bryan A. Franz [b]

[a] College of Marine Science, University of South Florida, St. Petersburg, FL 33701, USA
[b] NASA Goddard Space Flight Center, 8800 Greenbelt Road, Greenbelt, MD 20771, USA
[c] Science Systems and Applications Inc., 10210 Greenbelt Road, Lanham, MD 20706, USA

ARTICLE INFO

Editor: Menghua Wang

Keywords:
MODIS
VIIRS
Simultaneous nadir overpass
Calibration

ABSTRACT

Generation of consistent multi-sensor datasets is critical to the assessment of long-term global changes using satellite-borne instruments. Recent research suggests, however, that a fundamental assumption in satellite ocean color data processing concerning the calibration of the long near infrared band (i.e., 865 nm for MODIS) may introduce sensor-specific biases in space and/or time, which may also contribute to cross-sensor inconsistency in the derived reflectance data products. As such, it is necessary to assess the calibration of this band across sensors – performed here for MODIS/Aqua and VIIRS/SNPP using 'simultaneous same view' matchups (SSV; similar to simultaneous nadir overpass, but allowing for non-nadir measurements). Towards that end, we assess geometric, temporal, and spatial homogeneity metrics to identify SSVs, and develop a band-shifting approach applicable within standard satellite data processing routines to resolve expected spectral differences in the radiometry. We find top-of-atmosphere (TOA) radiance data from VIIRS/SNPP long near infrared band to be approximately 3% higher than the corresponding MODIS/A data. With the expectation that cross-calibrating the NIR_L should improve cross-sensor continuity of downstream geophysical products (e.g., chlorophyll-a), we reprocessed VIIRS data using updated calibration coefficients. While we noticed many minor improvements in cross-sensor continuity in such data products, large-scale geographic and temporal biases between these two datasets still remain. These discontinuities may be the result of disparate errors in polarization correction or atmospheric correction, both of which are modulated by radiant path geometry.

1. Introduction

Satellite ocean color instruments have provided otherwise unattainable data on spatial and temporal trends in the light field emanating from the world's oceans. However, the physical location of these sensors (on orbit) leads to difficulties in (1) discriminating oceanic from atmospheric signals in the measured total radiance signal; (2) calibrating and validating derived geophysical parameters (e.g., chlorophyll-a concentration; C_a); and (3) cross-calibrating multiple sensors towards longer-term datasets with minimal between-sensor uncertainties. Of these, the latter is particularly important in a climate context, as the usable life of any individual sensor (10 to 20 years at the absolute maximum) is likely too short to capture climate-scale variability (e.g., Lee et al., 2010).

Numerous previous works have investigated such climate-scale variability, using either single-sensor (Gregg et al., 2005; Henson et al., 2010; Siegel et al., 2013; Vantrepotte and Mélin, 2011) or merged-sensor (Gregg and Rousseaux, 2014; Lee et al., 2010; Signorini et al., 2015) datasets. These studies largely show no trend or a declining trend in global C_a, with large regional or basin-scale variability. Nevertheless, most of them note difficulties in statistical assessments of their respective datasets, owing to uncertainties in merging data from multiple sensors, or in drawing conclusions from datasets of too short duration. For example, Signorini et al. (Signorini et al., 2015) considered 16 years of MODIS/A [Moderate Resolution Imaging Spectroradiometer onboard Aqua] and SeaWiFS [Sea-viewing Wide Field-of-View Sensor onboard OrbView2] data. While they note general agreements between trends as derived using these two sensors (and a merged-sensor dataset), data from South Atlantic showed a positive trend using 11 years of SeaWiFS data, but a negative trend using either 11 years of MODIS data or the merged-sensor dataset. Gregg and Rousseaux (Gregg and Rousseaux, 2014) noted that C_a time series that switch from SeaWiFS to MODIS data

* Corresponding author.
E-mail address: bbarnes4@usf.edu (B.B. Barnes).

https://doi.org/10.1016/j.rse.2021.112439
Received 8 August 2020; Received in revised form 31 March 2021; Accepted 3 April 2021
Available online 17 April 2021

always showed a negative trend due to a bias between the sensors, and thereby recommended other techniques to reduce cross-sensor differences (Gregg and Casey, 2010). In contrast, for waters offshore China, Zhang et al. (Zhang et al., 2006) noted strong continuity (with no significant bias) in C_a between the same two sensors.

Such cross-sensor comparisons, by definition, require aggregations of large quantities of data, with globally and/or regionally averaged statistics obscuring the complexities of the differences between sensors (Djavidnia et al., 2010; Mélin, 2010). Indeed, Djavidna et al. (Djavidnia et al., 2010) found overall continuity between MODIS- and SeaWiFS-derived C_a, but noted significant modulations of this relationship both regionally and seasonally. Similarly, Melin et al. (Mélin et al., 2016) found spatiotemporal patterns of discontinuities between SeaWiFS, MODIS, and MERIS [Medium Resolution Imaging Spectrometer onboard Envisat] remote sensing reflectance (R_{rs}, in sr^{-1}) products. For demonstration of these discontinuities between MODIS and VIIRS/SNPP [Visible-Infrared Imaging Radiometer Suite (VIIRS) onboard the Suomi National Polar-orbiting Partnership (SNPP)], Fig. 1 shows the percent difference in R_{rs} and C_a as calculated using NASA default processing routines (specifically, [(MODIS-VIIRS)/MODIS], see Section 2.4. for processing details). Numerous potential sources of such discontinuities have been offered, including temporal differences in overpass times (Zhang et al., 2006), data quantity (Barnes and Hu, 2015), viewing geometry (Barnes and Hu, 2016), solar geometry (Djavidnia et al., 2010; Mélin et al., 2016; Zibordi et al., 2012), as well as C_a and aerosol optical thickness (Zibordi et al., 2012).

Amidst these potential sources of uncertainty, a fundamental assumption in system vicarious calibration (SVC) and atmospheric correction of satellite ocean color data concerns the long near infrared (NIR_L) band. In effect, the pre-launch calibration of the NIR_L band is considered sufficient for NASA's current operational SVC and AC procedures. This is supported by findings of Wang and Gordon (Wang and Gordon, 2002) that, based on radiative transfer simulations, moderate (±5%) errors in NIR_L calibration have minimal impacts (2–3%) on subsequently derived remote sensing reflectance (R_{rs}) in the visible wavelengths. As such, the gain (also termed g-factor; g) for the NIR_L band on any given sensor is not vicariously calibrated after launch, and is assigned a value of 1.0, with the radiance from this band then used "as-is" for calculation of atmospheric aerosol contributions to the measured total radiance prior to vicarious calibration of all other bands. While this overarching assumption may be true when performance is evaluated using discrete data points from either simulations or field measurements, recent research suggests that operational uncertainties resulting from this assumption are not equally distributed in space or time (Barnes et al., 2020).

The focus of this work is the intersection of noted cross-sensor differences in space and time (e.g., Fig. 1; Djavidnia et al., 2010; Mélin et al., 2016) and the sensitivity of R_{rs}(VIS) to $g(NIR_L)$ within individual sensor datasets (Barnes et al., 2020). As such, the overall objective of this work is to cross-calibrate the NIR_L bands of MODIS/A and VIIRS/SNPP using their on-orbit measurements over global oceans, specifically scaling VIIRS/SNPP to match MODIS/A. Throughout this process, we seek to objectively identify characteristics of MODIS / VIIRS pixel pairs that are appropriate for such cross-calibration. Following this, we assess the impacts of cross-calibrating these NIR_L bands on the continuity of downstream ocean color products including R_{rs} and C_a (Hu et al., 2012; O'Reilly et al., 2000), with the hypothesis that improving NIR_L cross-calibration will result in greater continuity of downstream products. A fundamental question behind this work is, if MODIS were to replace VIIRS on SNPP (or vice versa, if VIIRS were to replace MODIS on the Aqua satellite), would they measure identical top-of-atmosphere (TOA) radiance over the same ocean pixels?

2. Methods

2.1. Cross-calibration approach

Data from five ocean gyres, representing the "clearest ocean waters" (Morel et al., 2010) were used in this study (Fig. 2). Compared to coastal waters, gyre targets are desirable for cross-calibration work as they more likely (1) include negligible water leaving radiance in the NIR (i.e., black-pixel assumption; Gordon and Wang, 1994), (2) are spatially

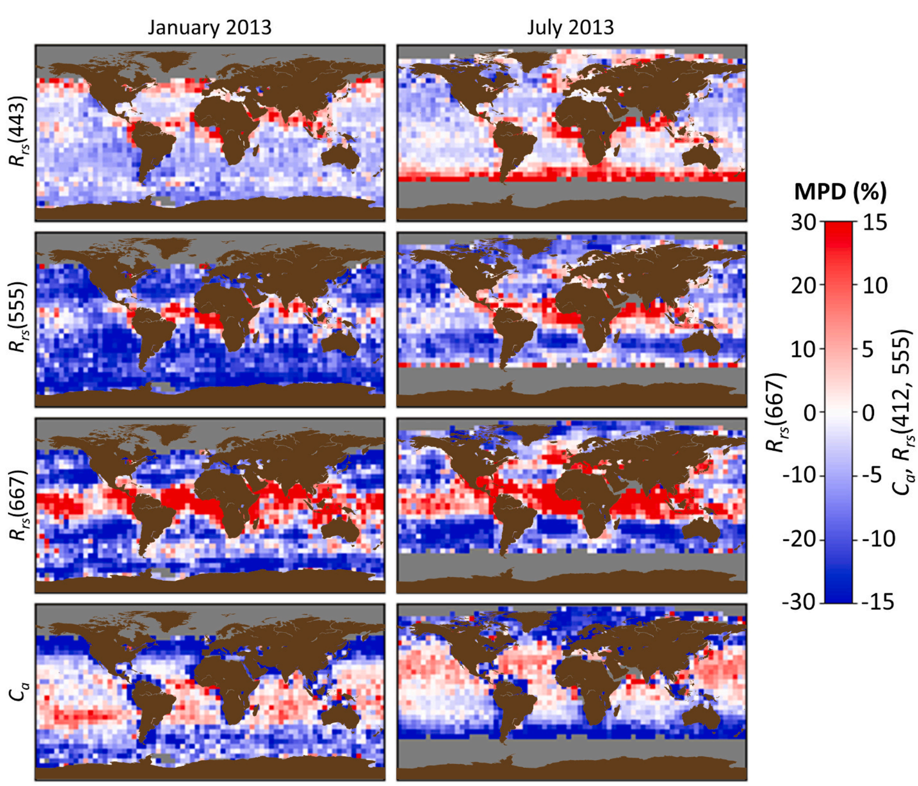

Fig. 1. Mean percent difference (MPD) between MODIS/A and VIIRS/SNPP for (top to bottom) $R_{rs}(443)$, $R_{rs}(555)$, $R_{rs}(667)$, and C_a during the time periods of (left) January 2013 and (right) July 2013, calculated at 5 degree spatial resolution. Empirical band shifts were implemented to calculate $R_{rs}(555)$ from $R_{rs}(547)$ and $R_{rs}(551)$ (NASA OBPG, n.d.), as well as $R_{rs}(667)$ from $R_{rs}(671)$ (Fig. S1). Positive values (reds) indicate VIIRS > MODIS. Note that the colorbar for $R_{rs}(667)$ spans twice the range of other products, commensurate with the smaller $R_{rs}(667)$ magnitude. Grey indicates no data, with brown landmask overlain. (For interpretation of the references to color in this figure legend, the reader is referred to the web version of this article.)

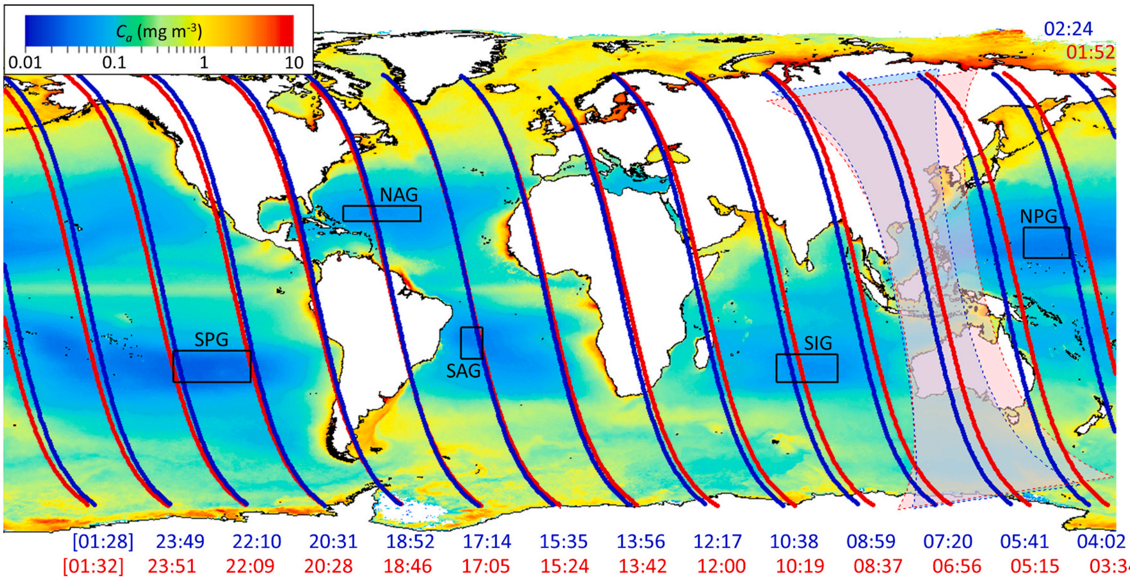

Fig. 2. Study areas (black boxes) and groundtracks for MODIS (blue) and VIIRS (red) on 16 January 2012 ("day 15" of the repeat orbits). Times (GMT) indicate approximate equatorial overpass time, with bracketed times being on the subsequent day ("day 0" of the repeat orbits). North Atlantic Gyre (NAG), North Pacific Gyre (NPG), South Pacific Gyre (SPG), South Atlantic Gyre (SAG), and South Indian Gyre (SIG) represent the "clearest ocean gyres" (Morel et al., 2010), as seen in the MODIS mission chlor_a composite (background). Land shown as white with black outline. Sample swaths shown for a single MODIS (light blue) and VIIRS (pink) overpass. Note all gyres except NPG have SSV on days with this groundtrack configuration. (For interpretation of the references to color in this figure legend, the reader is referred to the web version of this article.)

homogeneous, (3) are overlain by primarily marine aerosols, and (4) are less optically complex than coastal waters, reducing uncertainties in band shifting. Within these regions, we sought to identify pixels collected during simultaneous nadir overpasses (SNOs), as commonly used for multi-sensor assessment (Karlsson and Johansson, 2014; Li et al., 2015; Pahlevan et al., 2014; Uprety et al., 2013). For the determination of SNO in such analyses, thresholds defining the maximum ground distance and time between two nadir measurements are required. In the context of a scanning radiometer (e.g., MODIS and VIIRS), measurements at nadir are a tiny fraction of all data collected, with rigorous cross-sensor analyses requiring consideration of data from larger scan angles (Barnes and Hu, 2016). As such, we hereafter use the term 'simultaneous same view' (SSV) to define instances of collocated MODIS and VIIRS pixels which are 'essentially' coincident and have 'nearly' identical solar illumination geometry and satellite viewing geometry (collectively called radiant path geometry). As part of these analyses, and similar to the objectives of Chen et al. (Chen et al., 2020), we strove to define the vague terms 'essentially' and 'nearly' as used above via data-driven sensitivity analyses (see Section 2.3).

2.2. Optical framework

Our overall approach to estimate g(V862) used the MODIS/A 869 and VIIRS/SNPP 862 bands (hereafter termed M869 and V862, respectively). For pixels with identical location and geometry (including time), and assuming hypothetical sensors with identical bands (e.g., V862 and M862), g(V862) simply equals L_t(M862)/L_t(V862). In practice, there is no M862, and M869 cannot be used directly in this ratio because of the difference in path radiance at 869 nm and 862 nm. Thus, L_t(M'862) must be calculated [note, with this nomenclature, M869 and V862 are data directly from the specific sensors, while M'862 and V'862 are calculated].

The specifics of satellite ocean color atmospheric correction have been described and refined in numerous other publications over the last few decades (Bailey et al., 2010; Gordon and Wang, 1994). Here, we provide a brief synopsis of certain portions of that approach, particularly as implemented within the NASA ocean color processing software package SeaDAS/L2GEN (version 7.5), as necessary background to justify the rationale and methodological approach of the current study. As such, the basic decomposition of L_t (Franz et al., 2007; Gordon and Wang, 1994; Mobley et al., 2016) can be parameterized as:

$$L_t = \left[L_a + L_r + TL_g + tL_f + tL_w\right]^* t_{g_{sol}}{}^* t_{g_{sen}}{}^* p^* c_x \tag{1}$$

where L_a, L_r, L_g, L_f, and L_w are radiance contributions due to atmospheric aerosols, Rayleigh scattering, sunglint, white caps/foam, and water, respectively; T and t are Rayleigh-aerosol transmittance factors from the surface to the sensor (direct and diffuse, respectively); t_g is gaseous transmittance (from the Sun to the surface, *sol*, and from the surface to the sensor, *sen*); p is a polarization correction parameter, and c_x includes all instrument calibration coefficients. Note that this formulation ignores the spectral dependences which exist for all parameters. For the study areas (ocean gyre centers), the black pixel assumption [L_w(NIR) = 0] should nearly always be valid (Gordon and Clark, 1981), and pixels with detected L_w(NIR) (at the precision of the SeaDAS processing software) were excluded in the current study. Additionally, any pixels with substantial L_g or L_f contributions are generally not suitable for vicarious calibration studies - in the current study, we excluded any pixels for which SeaDAS returned non-zero values for L_g(NIR) or L_f(NIR). For any NIR band, this leaves:

$$L_t = [L_a + L_r]^* t_{g_{sol}}{}^* t_{g_{sen}}{}^* p^* c_x \tag{2}$$

Within SeaDAS, L_r is obtained from look-up-tables (LUTs, derived from radiative transfer simulations) as a function of wind speed (determined from National Centers for Environmental Prediction, NCEP), radiant path geometry, and sea-level pressure (Bodhaine et al., 1999; Wang, 2005). Polarization correction factors (p) are derived using prelaunch characterization of band-specific polarization sensitivity, combined with pixel specific radiant path geometry, L_r, and L_g (Meister et al., 2005; Mobley et al., 2016). Instrument calibration coefficients (c_x) are intended to ensure within-sensor continuity, and thus are a function of sensor temperature, scan angle, mirror side, detector, and time (Sun et al., 2014).

Gaseous transmittance factors (t_{gsol}, t_{gsen}) for the VIS and NIR bands primarily correct for the absorption due to atmospheric O_3, NO_2, and

H_2O, among others. Calculation of the former uses pixel specific radiant path geometry, [O_3] derived from ancillary sources (e.g., Ozone Monitoring Instrument, OMI), and band-specific (i.e., bandpass-integrated) O_3 attenuation coefficients (k_{O3}). For NO_2, t_{gsol} and t_{gsen} consider absorption in the upper (>200 m) atmosphere, with [NO_2] derived from climatological values within current operational OBPG processing. NCEP atmospheric precipitable water estimates are used to calculate water vapor transmittance via empirically derived band-specific polynomial coefficients. As most VIS and NIR ocean color bands are situated in spectral regions to avoid major water vapor absorption features, these primarily account for out-of-band effects (Gordon, 1995). An alternate model (using a different suite of polynomial coefficients) can be used for water vapor transmittance calculation in the SWIR (short-wave infrared) bands, which span water vapor absorption features (Franz, 2006). Note that $k_{NO2}$and k_{O3} (as used in calculating t_{gsol} and t_{gsen}) are quite small for NIR wavebands as compared to most VIS bands (Bogumil et al., 2003; Burkholder and Talukdar, 1994), meaning t_{gsol} and t_{gsen} for the data used in this study shows little deviation from 1 (~0.9992). All combined, for targets that meet the dark pixel assumption, all unknowns in Eq. (1) (except L_a) are calculated from ancillary or geometry information, and are thus not dependent on the satellite-measured radiance.

Within the currently operational NASA standard atmospheric correction, L_a is calculated on a pixel-by-pixel basis using radiance data from 'short' and 'long' wavebands in the near infrared (NIR_S and NIR_L, respectively, centered at 748 and 869 nm, respectively, for MODIS). Within this process, $L_a(NIR_S)$ and $L_a(NIR_L)$ are used along with 80 aerosol models which represent a range of bimodal aerosol size distributions inferred from AERONET [AERosol Observation NETwork] observations (Ahmad et al., 2010). These aerosol models (defined in LUTs) include the coefficients to convert between approximations for single- and multiple-scattering atmospheres, as well as the spectral shape of aerosol path radiance (Gordon and Wang, 1994). For the NIR_L and NIR_S wavebands at targets that meet the black pixel assumption, L_a is first calculated directly from L_t via Eq. (1). From this, for each aerosol model, the NIR single-scattering aerosol radiance (L_{as}) is then calculated. The average $L_{as}(NIR_S)$ / $L_{as}(NIR_L)$ ratio (termed ε), determined using all candidate models, is then used to select two models which most closely bracket ε. These two models, proportional to their relative proximity to ε, are used to extrapolate L_{as}(NIR) to L_{as}(VIS), and subsequently to convert L_{as}(VIS) to L_a(VIS). As such, within SeaDAS, L_a for all bands is a function of radiant path geometry, ancillary data, and $L_t(NIR_S$ and $NIR_L)$, and is thus calculated irrespective of the L_t measured for all other bands. The exception here is where the black-pixel assumption is not met, whereby an iterative approach is utilized to calculate $L_a(NIR_S$ and $NIR_L)$ (Bailey et al., 2010). This process does incorporate L_t information from bands outside the NIR, however, as mentioned above, such pixels are not considered in the current study.

2.3. Data processing

Due to the differences in path radiance between 869 and 862 nm, our approach to cross-calibrate MODIS and VIIRS NIR_L bands required band shifting. Building on the optical framework detailed in Section 2.2, this band shift was performed within SeaDAS. Recall that for the operational processing of MODIS data, L_t(M748) and L_t(M869) are used to select an atmospheric aerosol model, which establishes a spectral relationship for the aerosol path radiance that includes the points L_a(M748) and L_a(M869). L_a(862) lies along this curve, and, as is done for all other MODIS bands, L_a(M'862) can be calculated corresponding to the VIIRS 862 band characteristics. Within the current study, this was enacted within SeaDAS by modifying the M859 band characteristics to match those of V862, which forced the processing to calculate L_a(M'862) instead of L_a(M859).

To accomplish this, all relevant parameters [namely λ, F_0, and the out-of-band water vapor function coefficients (termed 'oobwv' in SeaDAS)] within the VIIRS sensor information file (msl12_sensor_info.dat in the SeaDAS distribution) were copied into the MODIS file at the M859 position (band #12). Of these, oobwv coefficients are not currently characterized in operational VIIRS processing, which is convenient for this cross-calibration approach. Note that many other values are included in the msl12_sensor_info.dat file, but these have no impact on the derived L_a(M'862) values. One exception is the water absorption transmittance function coefficients (seven coefficients, termed a_h20 – g_h20 in SeaDAS), which could impact L_a derivations. However, as this method is used only to calculate water vapor transmittance in the SWIR wavebands, the M859 and V862 coefficients were already equivalent (null) in their respective msl12_sensor_info.dat files.

Additionally, SeaDAS/L2GEN will return an error on initialization if not supplied with files containing Rayleigh LUTs (file prefix rayleigh_modisa in the SeaDAS distribution), polarization correction coefficients (p in Eq. (1); prefix polcor_modisa), and cross-calibration coefficients (c_x in Eq. (1); prefix xcal_modisa) for all band-center wavelengths indicated in the msl12_sensor_info.dat file. These coefficients are not used in derivation of L_a (except for pixels with L_w(NIR) > 0, as were explicitly excluded in this study), thus placeholder polcor_modisa, rayleigh_modisa, and xcal_modisa files with the appropriate 862 nm naming conventions were copied from other band-specific files already existing in their respective directories. After these combined changes, for every pixel, SeaDAS calculated L_a(M'862) instead of L_a(M859). Recall that this calculation is independent from the L_t(M859) as measured by MODIS. It is also important to reiterate that although this modified SeaDAS processing will return values for any requested product, only the L_a product in this false band should be considered valid, and only for pixels with null L_w(NIR). The veracity of changing SeaDAS processing in this manner can be verified by reproducing L_a for an existing MODIS band (e.g., 678 nm) at the M859 band position.

Satellite data processing for this work began with acquisition of all MODIS/A Level-1A and VIIRS/SNPP Level-1A granules (January 2012 – December 2018) intersecting the 5 gyres from NASA OBPG (Fig. 2). Using the modified MODIS sensor information file and the placeholder LUT files, these data were processed to Level-2 (L2), then mapped to a cylindrical equidistant projection at 1 km resolution using Python modules pyresample and pyproj, with gyre-specific boundaries of: North Atlantic Gyre (NAG; 70 W–45 W, 22 N–27 N), North Pacific Gyre (NPG; 150E-165E, 10 N–20 N), South Pacific Gyre (SPG; 125E-100E, 30S—20S), South Atlantic Gyre (SAG; 32 W–25 W, 22.5S–12.5S), and South Indian Gyre (SIG; 70E-90E, 30S—21S). During this mapping procedure, latitude / longitude grid cells were filled using a nearest neighbor approach in a two-stage fashion. First, the L2 scan line center nearest to each grid cell was identified, then each grid cell was filled with the nearest L2 pixel from that scan line. Products generated in this processing included all parameters in Eq. (1), as well as msec, scattering angle, and sensor zenith. At L2, we also calculated (and subsequently mapped) the coefficient of variation (CV) and max / min ratio (MMR) of the 3 × 3 box surrounding each non-flagged pixel. Note that no initial CV or MMR thresholds were implemented. At the time of processing (May–June 2019), all data and SeaDAS processing routines corresponded to NASA reprocessing R2018.0.

Collocated SSV matchups in this fully processed dataset were then identified using the following criteria:

1) To the precision reported in SeaDAS-derived Level-2 products, $L_g(M869) = L_f(M869) = L_g(V862) = L_f(V862) = 0$
2) For both sensors, grid cells not identified by L2 flags included in the L3 mask (enumerated below)
3) For both sensors, grid cells not within a 20 × 20 box surrounding any pixel identified as CLDICE
4) Absolute time difference between MODIS and VIIRS measurements (|ΔTime|) < 30 min
5) Senz for both MODIS and VIIRS <30°
6) Absolute Senz difference between MODIS and VIIRS (|ΔSenz|) < 5°

7) Absolute scattering angle difference between MODIS and VIIRS ($|\Delta$ Scat$| < 5°$

All said, 14 'overpasses matches' (gyre, orbital cycle day, and time combinations) showed instances of SSV according to geometry alone (items 4–7, above; Fig. 3). Due to slight orbital variations, not every overpass match included potential SSV during every instance of the 16-day repeating orbital cycles. Beyond sensor geometry, the following L2 flags (item 2, above) were used to identify pixels which were unsuitable for subsequent analyses: ATMFAIL, LAND, HIGLINT, HILT, HISATZEN, STRAYLIGHT, CLDICE, COCCOLITH, HISOLZEN, LOWLW, CHLFAIL, NAVWARN, ABSAER, MAXAERITER, ATMWARN, and NAVFAIL. These flags are those used to mask Level-3 R_{rs} composites (https://oceancolor.gsfc.nasa.gov/atbd/ocl2flags/). A dilation of 20 km was applied for any grid cells identified as CLDICE, as memory and adjacency effects for L_t were expected to be larger than those for R_{rs} (item 3, above) (Feng and Hu, 2016).

Fig. 4 shows variability in these geometric data products as commonly observed in granule pairs, as well as the impact of various data exclusion techniques. From the resulting data, we assessed basic summary statistics [particularly median and median absolute deviation (MAD)] of the dataset as a whole and after culling the data by individually restricting the threshold criteria numbered 4–7. Additionally, these summary statistics were calculated after excluding data that did not meet increasingly tightening spatial homogeneity thresholds (MMR or CV), as well as thresholds for relative azimuth and sensor azimuth. In doing so, we expected that (1) tightening threshold criteria for SSV determination would decrease data quantity; while (2) 'improvement' to the dataset could be identified by progressively lower MAD. In other words, we attempted to identify SSV metrics for which tightening the threshold preferentially excluded outliers in the dataset.

2.4. Assessment of geophysical products

Previous studies (Pahlevan et al., 2017b; Sayer et al., 2017) assessing calibration between MODIS/A and VIIRS/SNPP have found differences

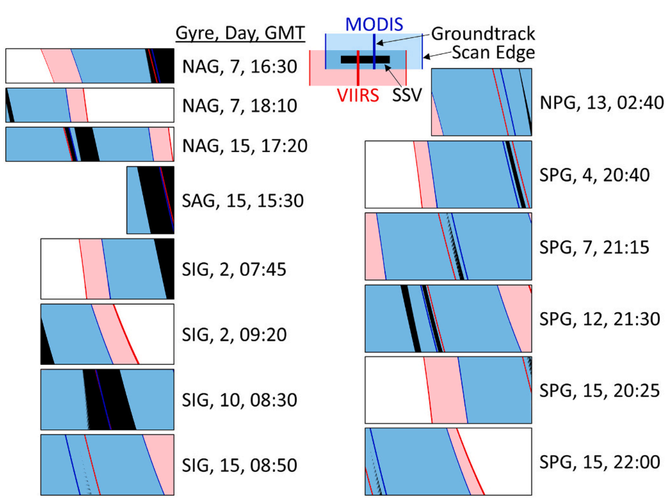

Fig. 3. MODIS and VIIRS groundtracks (blue and red, respectively), swaths (semi-transparent light blue and pink, respectively), and SSV (black) for all gyre/day/time combinations with potential SSV (termed 'overpass matches'). Scale is identical for all panels. "Day" indicates date number of the repeat orbital cycle (starting 1 January 2012). Note that for these locations and overpass matches, VIIRS swaths completely overlay MODIS swaths, thus no unique MODIS swath data (transparent light blue) are visible. Also, due to orbital variability and clouds, SSV pixels are not always present for each overpass match (e.g., SSV were only observed on 6 out of 159 instances of SIG, 15, 08:50). (For interpretation of the references to color in this figure legend, the reader is referred to the web version of this article.)

of approximately 3–3.5% for their respective NIR_L bands. Assuming g(M869) = 1.000 (the current operational default), application of this calibration correction to VIIRS would yield g(V862) ≈ 0.965–0.97. Using the approach of Franz et al. (Franz et al., 2007) and considering a new g(V862) = 0.97 to be the 'pre-launch' vicarious gain, we calculated SVC gains for all other VIIRS bands in the visible and NIR (Table 1). As detailed in Franz et al. (Franz et al., 2007), this process included (1) initial assumption of the $g(NIR_L)$ value, (2) calculation of $g(NIR_S)$ using VIIRS data from the South Pacific Gyre ($N = 789$), and (3) subsequent calibration of all other bands against MOBY (Marine Optical Buoy, Brown et al., 2007) data ($N = 223$) propagated to L_t using the aerosol radiance model determined using VIIRS $L_{as}(NIR_L$ and $NIR_S)$. Note that these SVC gains were calculated via the same processing code and data selection/exclusion criteria used in operational processing. As such, repeating this procedure with $g(862) = 1.00$ exactly replicated the extant operational SVC gains for all bands. We subsequently acquired all 2013 VIIRS/SNPP L1B and GEO files from NASA OBPG and processed them to Level-2 using this alternate gain configuration, with the resulting dataset being termed $VIIRS_{ALT}$. These files were merged into daily Level-3 BIN files. Additionally, all 2013 daily Level-3 MODIS/A and VIIRS/SNPP ($VIIRS_{ORG}$) BIN files were acquired from NASA OBPG (these use the current default SVC gains, and were used in creation of Fig. 1).

These daily resolution BIN files were mapped to standard mapped image (SMI) format at 4 km resolution, whereby the average and pixel count within each bin was determined for R_{rs}(VIS) and chlor_a. Bins (4 km daily) which included no data in any of the three datasets (MODIS, $VIIRS_{ORG}$, and $VIIRS_{ALT}$) were excluded from all further analysis. For proper comparison, M547 and V551 were converted to M'555 and V'555, respectively, as performed in SeaDAS ((NASA OBPG, n.d.). Additionally, V'667 was calculated from V671 using an empirical relationship derived from SeaBASS (Werdell and Bailey, 2005) data. Specifically, all R_{rs} spectra within the SeaBASS dataset (accessed on 24 December 2020) which included values at both 667 nm and 671 nm (±1 nm) were extracted ($N = 3183$). These data were transformed into log-space, and simple linear regression was used to derive the following relationship:$R_{rs}(667) = 10^{(1.0048\ \log(R_{rs}(671))+0.0056)}$; with $R^2 = 0.99$ (Fig. S1). Monthly data were calculated using the daily SMI images via weighted averages. To compare VIIRS and MODIS products, we calculated mean percent difference (MPD) as

$$\mathrm{MPD} = \frac{100^{*}\left(\overline{\mathrm{VIIRS}} - \overline{\mathrm{MODIS}}\right)}{\overline{\mathrm{MODIS}},} \tag{3}$$

with the overbar representing the mean for any given spatiotemporal bin (e.g., monthly 5 degree box, as in Fig. 1). While unbiased percent difference is more typically used in satellite intercomparisons (Barnes et al., 2019; Mélin and Franz, 2014), here we consider change against a single reference (MODIS). This allows relative cross calibration of $VIIRS_{ORG}$ and $VIIRS_{ALT}$ against MODIS data to be calculated using the change in absolute mean percent difference ($\Delta|\mathrm{MPD}|$), whereby.

$$\Delta|\mathrm{MPD}| = |\mathrm{MPD}_{\mathrm{VIIRS\_ORG}}| - |\mathrm{MPD}_{\mathrm{VIIRS\_ALT}}| \tag{4}$$

Note |MPD| is distinct from the more commonly used MAPD (mean absolute percent difference). Negative values in $\Delta|\mathrm{MPD}|$ indicate tighter consistency between MODIS and $VIIRS_{ORG}$, while positive values show improvement in cross-sensor consistency using the alternate VIIRS gains.

3. Results

While SSV were identified in each of the 14 overpass matches (Fig. 3), the quantity of SSV data differed greatly by gyre. Only two dates contained SSV in the NPG, with total data quantity of 4316 matchups. As such, NPG data are often excluded in subsequent analyses and discussion. Despite the SAG having only one overpass match, 40 dates of this

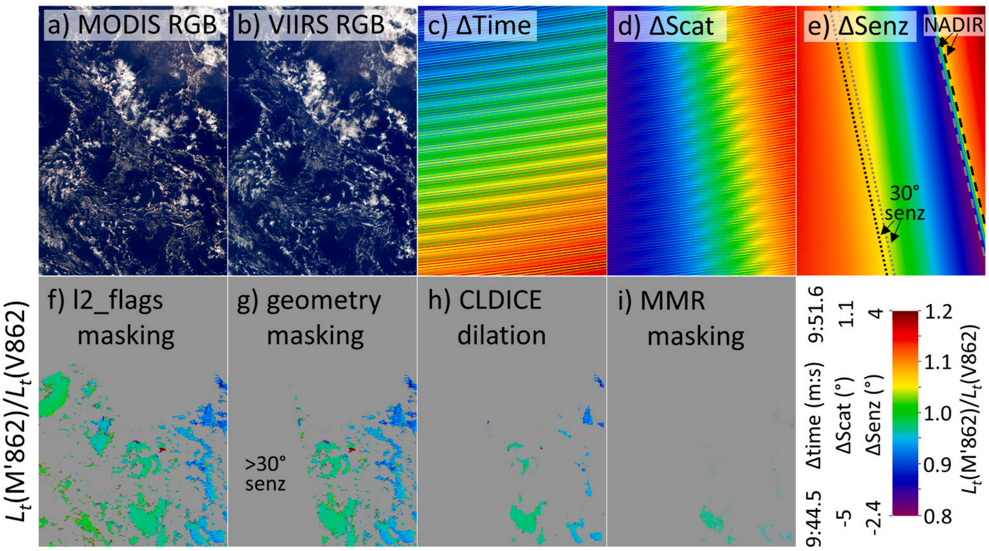

Fig. 4. MODIS and VIIRS data collected on 19 June 2016 within the SAG under SSV conditions. Top row shows (a-b) true color RGB composites; (c) difference in time between measurements (in m:s); (d) difference in scattering angle (°); (e) difference in sensor zenith (°) with nadir (dashed lines) and 30° sensor zenith (dotted lines) for MODIS (grey) and VIIRS (black) demarcated. Bottom row shows L_t(M'862)/L_t(V862). The same data are included in all panels, but are masked using progressively more restrictive criteria: (f) masking any pixels indicated by noted Level-2 processing flags; (g) additionally masking pixels exceeding SSV thresholds (in this instance, only the Senz threshold is exceeded); (h) masking pixels within 20 km of CLDICE pixels; and (i) masking pixels with high spatial heterogeneity in L_t(M'862) or L_t(V862). Colorscale for (c)-(e) are to the left of the colorbar in the bottom right panel.

Table 1
Vicarious gains for VIIRS/SNPP (R2018.0) with $g(862) = 1.00$ (current default) and 0.97.

Band (nm)	410	443	486	551	671	745	862
Original gains	0.9752	0.9579	0.9874	0.9824	0.9918	0.9922	1.0
Alternate gains	0.9748	0.9558	0.9834	0.9744	0.9764	0.9712	0.97
Alternate gain σ	0.0135	0.0128	0.0133	0.0010	0.0063	0.0153	–

overpass match included SSV, with total data quantity of 3.6E5 matchups. This is similar to the data quantity in SPG (4.6E5), where SSV were spread out over 123 dates and between 5 different overpass matches. Data quantity was greatest in the NAG (1.4E6 in 237 dates) and especially the SIG (5.9E6 in 250 dates), and in the respective (austral or boreal) wintertime for each gyre (Fig. 5).

The median and MAD for the L_t(M'862)/L_t(V862) ratio, calculated for each date with SSV pixels, are shown in Fig. 6. Most medians (65%) are between 0.90 and 1.05, and most MAD (89%) are <0.05. The spread of these medians varies substantially by gyre, with values in SAG and especially SPG being more variable than the other two gyres. In the aggregate, MAD values are also higher in these two gyres. Not surprisingly, dates with fewer SSV matchups generally show more variability in the median values and often larger MAD. Gyre-specific median L_t(M'862)/L_t(V862), calculated using all matchups within each gyre, ranged from 0.95 in SAG to 0.979 in NAG.

We subsequently sought to refine thresholds used to identify SSV matchups, with the expectation that the variability in L_t(M'862)/L_t(V862), quantified as MAD, should be reduced when tightening relevant metrics. A graphical representation of this analysis is presented in Fig. 7. For all of the initially used geographic criteria (items 4–7 in the list in Section 2.3., columns 3–6 in Fig. 7), no widespread decrease in MAD was identified with progressively tightening thresholds. For example, our initial SSV threshold excluded any pixels with MODIS or VIIRS Senz >30°. If we had, alternately, selected 15° as this threshold, our data quantity would have been approximately half (including no NPG data), gyre-specific MAD would be largely unchanged, and the determined gyre-specific gains [the median of L_t(M'862)/L_t(V862)]

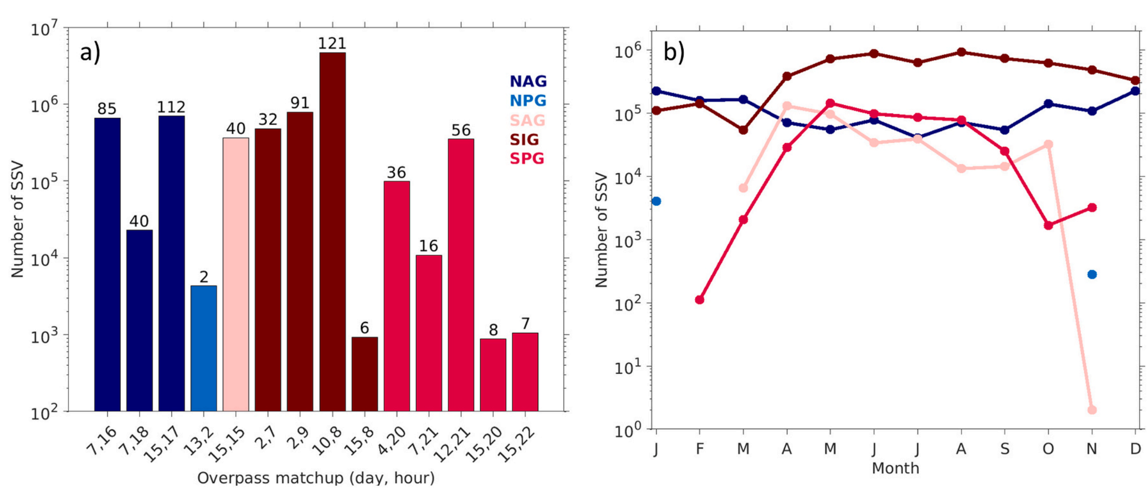

Fig. 5. Histograms of SSV matchups (after l2_flags masking and CLDICE dilation) according to (a) overpass matchups (see Fig. 3) and (b) binning by month. Numbers above bars indicate the number of overpass matchups with at least one SSV (out of ~159). Note logarithmic scale for y-axes.

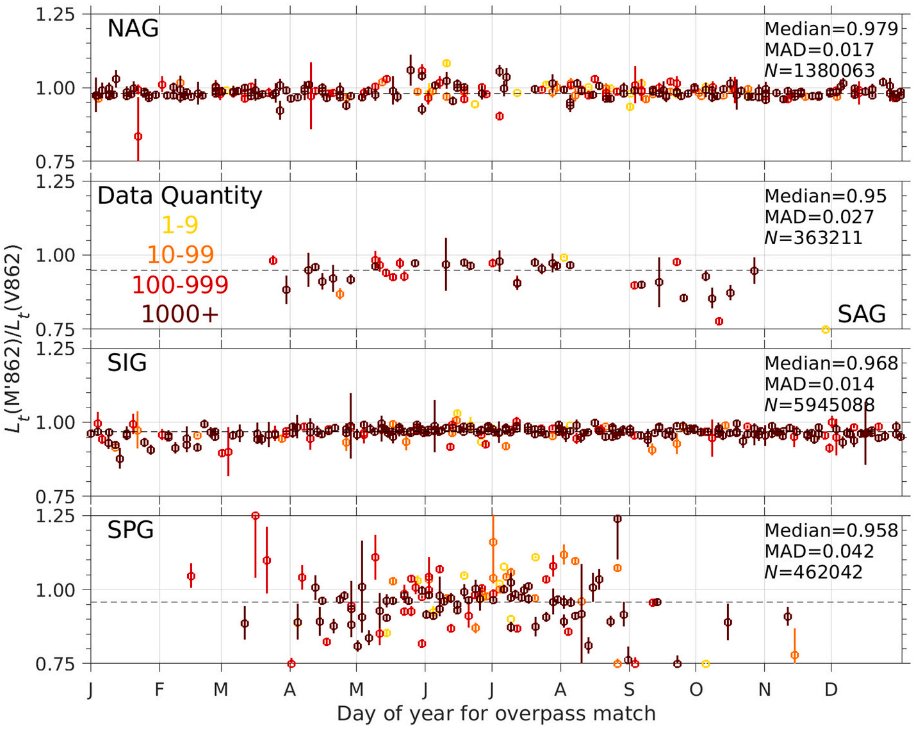

Fig. 6. Median L_t(M'862)/L_t(V862) (circles) with 1 median absolute deviation error bars for SSV within each overpass match (2011–2018). Data from four gyre regions (NPG only had two dates with SSV) are shown according to day of year. Color indicates number of SSV with each overpass match: <10 (yellow), 10–99 (orange), 100–999 (red), ≥1000 (maroon). For each gyre, dotted line shows overall median L_t(M'862)/L_t(V862). Annotations on top right of each panel show statistics for all SSV within each individual gyre. (For interpretation of the references to color in this figure legend, the reader is referred to the web version of this article.)

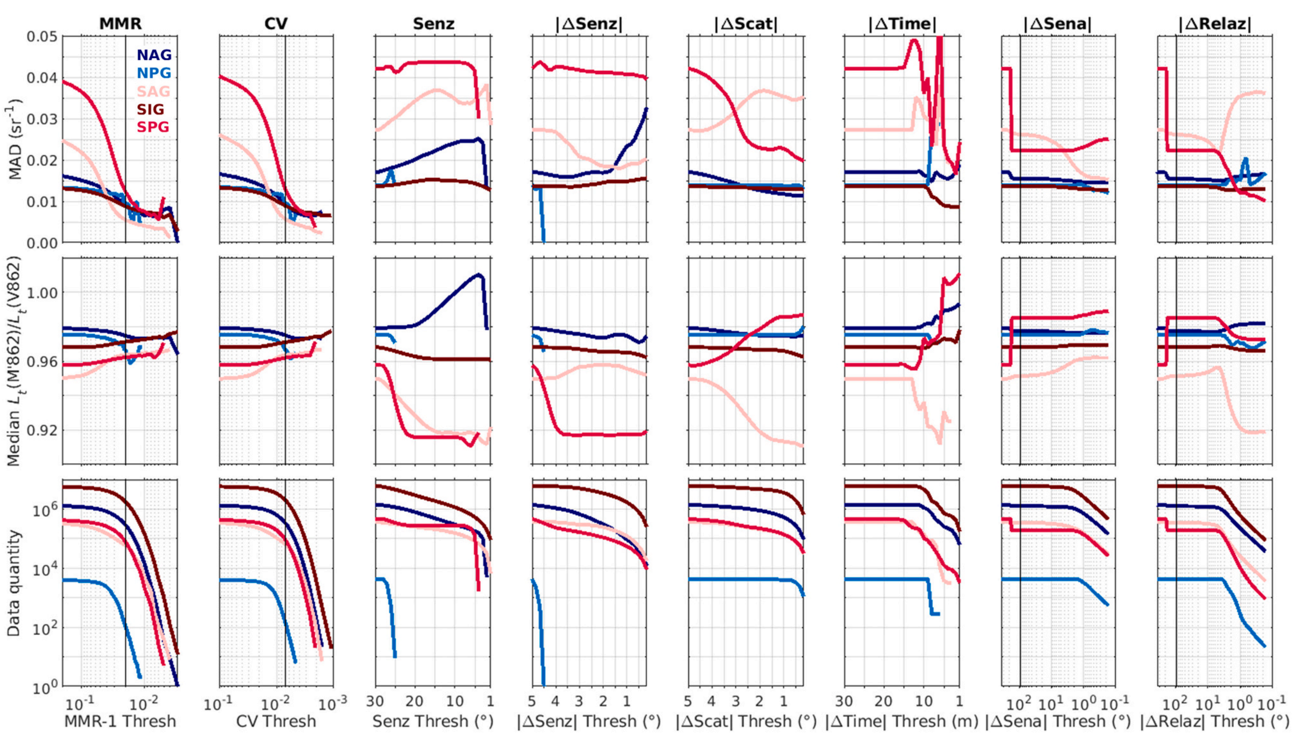

Fig. 7. Gyre-specific impacts of tightening SSV criteria on (top row) median absolute deviation of L_t(M'862)/L_t(V862), (middle row) median L_t(M'862)/L_t(V862), and (bottom row) SSV data quantity. Columns show (left to right) max/min ratio (less 1 to allow for log plot), coefficient of variation, sensor zenith, absolute difference in sensor zenith between SSV pixels, absolute difference in scattering angle, absolute difference in time, absolute difference in relative azimuth, and absolute difference in solar azimuth. Within all panels, criteria are least restrictive on the left side, and get progressively tighter moving rightward. Note logarithmic x-axis for columns 1, 2, 7, and 8. Vertical bars in 1, 2, 7 and 8 represent thresholds which maximize data quantity and agreement (1.02, 0.007, 90°, and 90°, respectively).

would vary from 0.92 to 0.99. Two additional geometric parameters were also assessed, namely the absolute differences in sensor azimuth (Sena) and relative azimuth (Relaz) between MODIS and VIIRS (Fig. 7 columns 7 and 8, respectively). For both, we note generally decreasing MAD with tightening thresholds, most prominently in SPG for absolute difference thresholds of roughly 195–165°. NAG data showed similar sharp improvement with tightening of |ΔSena| or |ΔRelaz| thresholds between 224 and 143°, while steady degreases in MAD were seen in SPG data with |ΔSena| or |ΔRelaz| thresholds tightening from 239 to 0° or 243–5°, respectively. Tightening the |ΔSena| or |ΔRelaz| thresholds below ~5°, however, was associated with MAD increases in SPG or SAG, respectively. In addition, while the threshold assessments shown in Fig. 7 primarily are represented via absolute differences (with the exception of Senz; column 3), we also tested tightening of the raw (single sensor) geometry values, and note a general lack of consistently decreasing MAD with tightening criteria.

In contrast to these temporal and radiant path geometry metrics, tightening the metrics of spatial homogeneity was a consistently effective method by which to reduce the variability in the datasets. For both MMR and CV, as the metric was tightened, MAD showed steep declines within all gyres (especially SPG and SAG). At MMR and CV thresholds of 1.02 and 0.007, respectively, data quantities are approximately half that of the full dataset, while MAD for all gyres is ~0.01 and gyre-specific median ranges from ~0.96 to 0.975.

From these results, we excluded data for which (1) MMR > 1.02 or (2) |ΔRelaz| > 90°. We then recalculated the date-specific MAD and median (Fig. 8; Fig. S2 also shows these results separated by year and season). The spread of median values among the individual dates with SSV was noticeably reduced, as were the MAD values about those medians. In contrast to the full dataset (Fig. 6), the SPG medians of this refined dataset are not substantially more variable than the other gyres. Data quantity appears to influence the spread of these data in two ways. First, medians on dates with fewer SSV regularly show large deviations from the overall gyre-specific medians, similar to that seen for the full dataset. Additionally, time periods with fewer SSV (e.g., March – July in the NAG) tend to show increased variability in the date-specific medians. Median L_t(M'862)/L_t(V862) within individual gyres varied from 0.964 to 0.974, with the overall cross-gyre median being 0.971 ± 0.0088.

4. Discussion

Our analysis of all matchups which met the initial criteria for SSV showed general agreement between the gyres as to the median L_t(M'862)/L_t(V862) (0.95–0.98), with more substantial variability in MAD (Fig. 6). Of all the parameters tested, tightening of the spatial homogeneity metrics (CV and MMR) showed the most prominent impacts on MAD, with all gyres showing steady decreases with more stringent heterogeneity thresholds (Fig. 7). From this, we determined that an MMR threshold of 1.02 or a CV threshold of 0.007 were equally acceptable. To a lesser extent, tightening |ΔRelaz| and |ΔSena| also showed utility in culling data, particularly in SPG. This improvement reversed for certain gyres below a threshold of ~5°, coincident with the greatest quantity of data. As such, we instituted a conservative |ΔRelaz| threshold of 90°, but recognized almost negligible differences in results if this threshold were placed anywhere between 10° and 140°. The 90° threshold takes advantage of the initial obvious MAD improvements, especially in SPG (Fig. 7), without requiring a more subjective determination of a lower boundary.

It is important to note that our operationalization of 'improvement' in data spread only included decreases in MAD – not inter-gyre differences in MAD or median L_t(M'862)/L_t(V862) values. Nevertheless, gyre specific values for both the MAD and median L_t(M'862)/L_t(V862) also converged with tightening spatial homogeneity and |ΔRelaz| criteria. This cross-gyre agreement reinforces our confidence in both the methodology and the resultant findings.

Most of the geometry thresholds showed no consistent utility in culling outliers from these data (Fig. 7). Indeed, many gyres showed increases in MAD with tightening geometry thresholds. This is somewhat unexpected, as pixels with identical viewing geometry should,

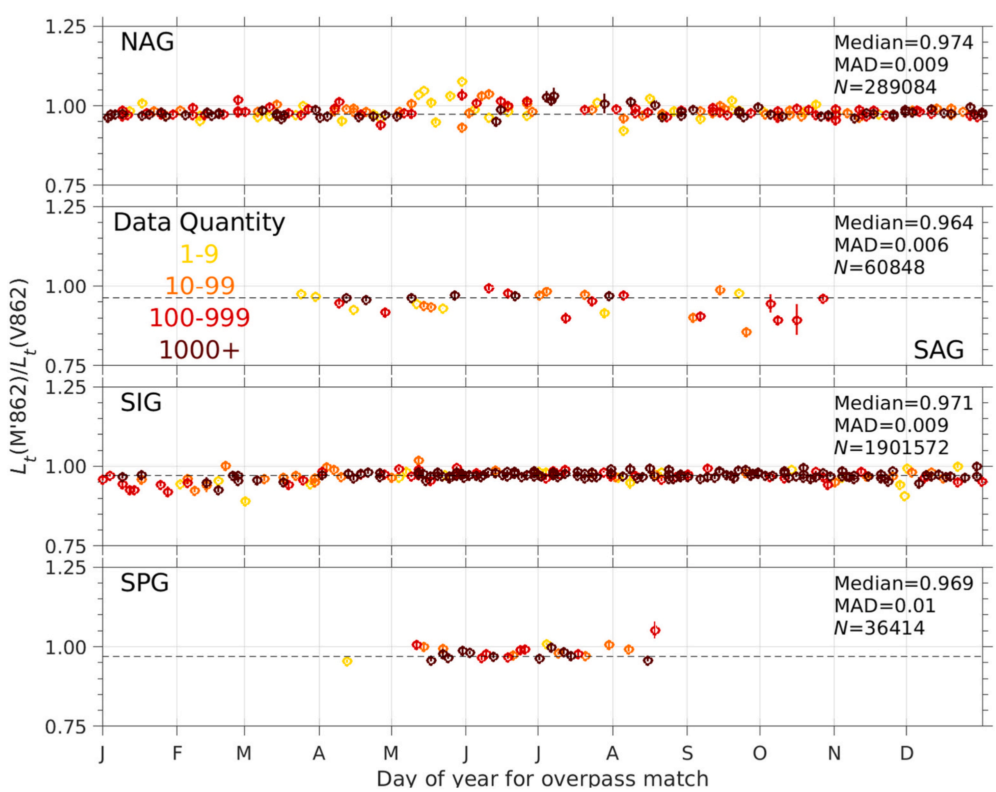

Fig. 8. Same as Fig. 6, but only showing data with MMR < 1.02 and |ΔRelaz| < 90°.

theoretically, have smaller differences in path radiance than those with divergent viewing geometry (since these matchups are collocated, L_w should be identical). Noting the strong impact of the spatial homogeneity metrics, we subsequently assessed impacts of tightening geometry thresholds on data which had already been culled by the spatial homogeneity thresholds (with and without the |ΔRelaz| threshold), but again found no consistent impacts. Similarly, we also graphically assessed 2D—4D impacts of tightening thresholds, attempting to identify combinations of tightening geometry thresholds which improved MAD for all gyres (for example, if MAD improvements were seen with tightening ΔSenz only for pixels with Senz <10° and ΔScat <5°). Again, however, no widespread positive impacts of tightening geometry thresholds were observed. Apart from the |ΔRelaz| and |ΔSena| analyses already mentioned, the one exception within all of this discussion was for the Senz threshold. As seen in Fig. 7, column 3, and numerous other visualizations of data subsets, MAD typically increased or stayed stable as the Senz threshold was tightened from 30° to 5°, but striking decreases in MAD were observed as this threshold was further tightened below 5°. The data quantity with such a stringent Senz threshold was quite low, and the improvements in MAD often did not counter the MAD increases observed with the initial threshold tightening from 30° – 5°.

Having said that, these analyses likely indicate that the initial geometry thresholds are sufficient, if not potentially too stringent, for satellite cross-calibration over ocean targets, but should be accompanied by a |ΔRelaz| (or |ΔSena|) threshold of ~90°. The necessity of this threshold is understandable in a geometric context – large differences in Relaz or Sena between sensors indicates viewing a target from opposite directions (e.g., MODIS viewing a pixel from the East, with VIIRS viewing from the West; for example, overpass match SPG, 7, 21:15 in Fig. 3; (Pahlevan et al., 2016). Note that this condition was common for SPG and, to a lesser extent, SAG and NAG (Fig. 3), which were the only gyres where |ΔRelaz| and |ΔSena| thresholds had substantial impacts (Fig. 7). Additionally, while the spatial heterogeneity metrics showed utility in culling outliers for all gyres, gyre-specific differences in said utility can be understood in the context of L_t magnitude. For the full dataset, median L_t in SAG (2.1 W m^{-2} sr^{-1} for MODIS) and especially SPG (1.8 W m^{-2} sr^{-1} for MODIS) was substantially lower than for the other gyres (medians of 2.4–3.0 W m^{-2} sr^{-1} for MODIS). Assuming relatively consistent L_t noise between gyres, lower L_t magnitude would mathematically lead to a more variable L_t/L_t ratio, thus the higher MAD in SAG and SPG for the full SSV dataset (Fig. 7). The MMR and CV metrics, both of which are implicitly scaled to the magnitude of the original dataset, should thus have greater impacts in SAG and SPG, as was observed. As SPG data are solely used in SVC of NIR$_S$ band, it is critical that spatial heterogeneity metrics continue to be implemented within operational SVC processes (Franz et al., 2007).

These results complement those of Chen et al. (Chen et al., 2020), who established cross-sensor geometry thresholds towards cross-calibration of VIIRS and MERSI-II (Medium Resolution Spectral Imager II onboard Fengyun-3D). Within that work, the SeaDAS LUTs were used to simulate L_t(VIS) for the full suite of potential satellite radiant path geometry conditions, from which percent relative differences in L_t(VIS) between geometry conditions were calculated. The geometry threshold results presented in the current study fit within those of Chen et al. (Chen et al., 2020), but also highlight that generic thresholds based on the suite of all possible geometries may not be acutely suited for SSV optimization within a specific dataset. For example, Chen et al. (Chen et al., 2020) specify an interplay between the solar zenith maximum threshold and the ΔSolz threshold, noting that a lower-than-desired Solz threshold (50°) was selected so that the ΔSolz threshold would not have to be too small (they eventually settled on 2.9°). Although some of our SSV data lie outside those thresholds, all appear to be within geometries which would be deemed 'acceptable' according to the basis for Chen et al. (Chen et al., 2020) threshold determinations (i.e., ±2.5% relative difference; compare the SSV histograms in Fig. S3c to relative difference representations in Fig. 5 of Chen et al. (Chen et al., 2020)). As such, the data-driven approach described in this paper may be considered a more flexible approach to derive tailored thresholds for data culling, which may be especially relevant for satellite intercomparisons with limited data quantity, such as Landsat-class missions (Pahlevan et al., 2017b).

From the cross-calibration results between M869 and V862, we find a difference of approximately 3%. Pahlevan et al., (Pahlevan et al., 2017b) performed cross-calibration of the NIR$_L$ bands between Landsat-8 OLI and both MODIS and VIIRS, finding minimal differences between OLI 865 and MODIS 869. However, VIIRS L_t(862) were roughly 3.5% higher than OLI 865, which they postulated could indicate a mismatch between MODIS and VIIRS. Additionally, Sayer et al., (Sayer et al., 2017) performed a more direct comparison of MODIS and VIIRS SNO using 'dark water' pixels, and calculated g(V862) = 0.963 (±0.004). Both of these studies used varying approaches, which also differ from the current study, for (1) atmospheric correction, (2) band shifting, and (3) identification of SNO pixels acceptable for inclusion in analyses. While the difference between the MODIS and VIIRS NIR$_L$ bands (as calculated in the current study) is slightly less than that as calculated in either Pahlevan et al., (Pahlevan et al., 2017b) or Sayer et al., (Sayer et al., 2017), it is within listed error ranges. We also note that 2018 was an anomalously high year in our dataset, and that the instrument calibration for the MODIS dataset used in the current study (R2018.0) has recently been modified to account for calibration errors after March 2018 (https://oceancolor.gsfc.nasa.gov/reprocessing/). Excluding 2018 data, median L_t(M'862)/L_t(V862) was 0.969 ± 0.0078 (Fig. S2). Our findings, together with these previous studies, indicate robustness of the calculation of a ~ 3–3.5% difference between MODIS and VIIRS NIR$_L$ bands. In the context of vicarious calibration of satellite ocean color data, this ~0.5% spread in g(NIR$_L$) will likely have minor impacts on R_{rs} retrievals in the visible bands (Barnes et al., 2020; Wang and Gordon, 2002).

As such, we calculated an alternate suite of gains for VIIRS/SNPP via the Franz et al. (Franz et al., 2007) approach, except using g(862) = 0.97 (Table 1). Using this gain suite, we re-processed all L2 files collected by VIIRS in 2013 and calculated MPD against MODIS/A data (Eq. (3)). Additionally, using the Δ|MPD| parameter (Eq. (4), Fig. 9), we identified any improvements or declines in cross-sensor continuity resulting from using this alternate VIIRS dataset, as opposed to that calculated using the default VIIRS calibration (Fig. 1). As such, Fig. 9 shows substantial variability in Δ|MPD| by data product and season. Specifically, R_{rs}(443) shows general 0–2% improvement in most seasons, but 2–4% declines in regions with exceptionally high solar zenith (i.e., Artic region in January, Antarctic in July). Variability in Δ|MPD| was also observed according to both geographic and seasonal comparisons of R_{rs} in the 555′ and 667/667′ bands. Specifically, general improvements were noted with higher zenith angles, as well as in the equatorial regions (restricted to equatorial Atlantic and Indian regions for 555′). Improvement was more widespread in for the red bands. C_a shows moderate improvement in equatorial and tropical regions using the alternate VIIRS gains, but substantial widespread decreases in higher latitudes. Several global regions show reduced cross-sensor agreement in C_a despite improvement (or no change) in cross-sensor agreement of the precursor R_{rs} bands shown. For waters with C_a > 0.20, chlor_a retrievals depend on the maximal value between R_{rs}(443) and R_{rs}(M488 or V490), thus these discrepancies may result from switching of the 'blue' band in C_a calculation (https://oceancolor.gsfc.nasa.gov/atbd/chlor_a/).

Combining Figs. 1 and 9, the changes in MODIS/VIIRS MPD resulting from the use of VIIRS$_{ALT}$ can be used to visualize the primary direction of change in the original geophysical products. For instance, R_{rs}(443) MODIS/VIIRS$_{ORG}$ MPD is highly positive (MODIS 10% or more higher than VIIRS) for the regions with extremely high solar zenith angle, but slightly negative in most other regions (Fig. 1). As noted above, Δ|MPD| for this band is negative in these high solar zenith locations, but positive most everywhere else (Fig. 9). In short, where VIIRS$_{ORG}$ > MODIS, VIIRS$_{ALT}$ > > MODIS, and where VIIRS$_{ORG}$ < MODIS, VIIRS$_{ALT}$ ≥

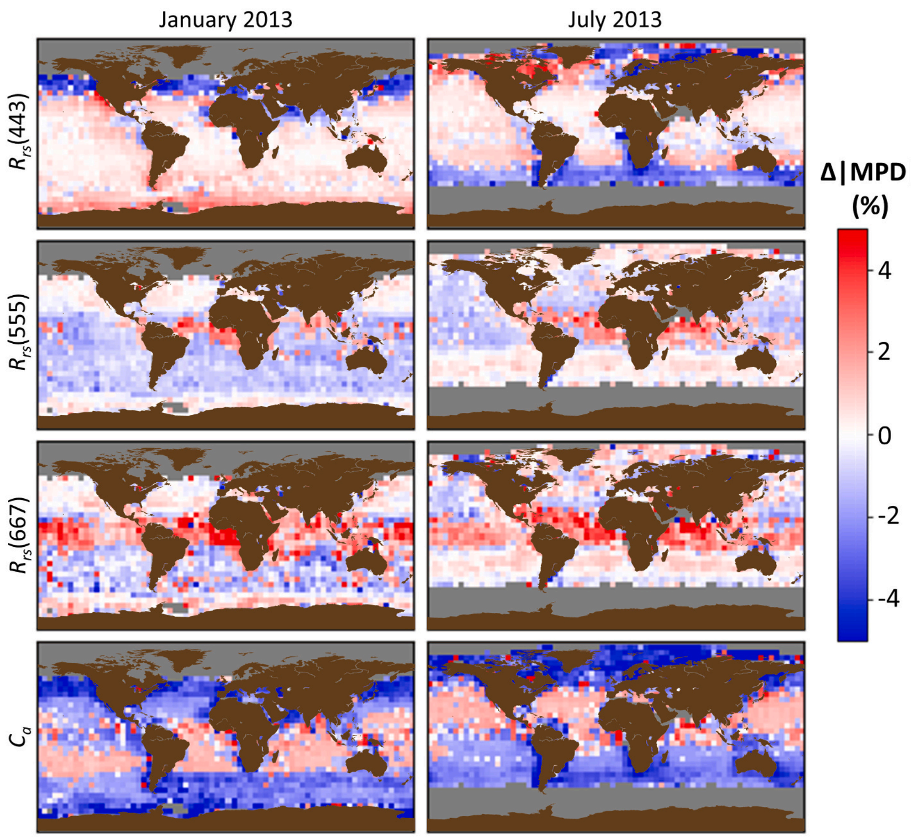

Fig. 9. Impacts of modified VIIRS gains on agreement between MODIS and VIIRS for various ocean color products, displayed as the change in absolute percent difference (Δ|MPD|) between MODIS and VIIRS after transitioning from $VIIRS_{ORG}$ to $VIIRS_{ALT}$. Data shown for (top to bottom) $R_{rs}(443)$, $R_{rs}(555)$, $R_{rs}(667)$, and C_a during the time periods of (left) January 2013 and (right) July 2013 at 5 degree spatial resolution. Positive values (reds) indicate improvements in the consistency of $VIIRS_{ALT}$ and MODIS as compared to $VIIRS_{ORG}$ and MODIS. Grey indicates no data, with brown landmask overlain. (For interpretation of the references to color in this figure legend, the reader is referred to the web version of this article.)

MODIS. Thus, for $R_{rs}(443)$, $VIIRS_{ALT}$ is generally greater than $VIIRS_{ORG}$. This relationship is more variable for the other R_{rs} bands, as differences in trend emerge between equatorial and high solar zenith regions. Specifically, for these bands, $VIIRS_{ALT} < VIIRS_{ORG}$ in the equatorial regions, but $VIIRS_{ALT} > VIIRS_{ORG}$ in the higher latitudes. For most of the globe, $VIIRS_{ALT}$ C_a < $VIIRS_{ORG}$ C_a.

Overall, we note general improvement in MODIS/VIIRS continuity resulting from the use of $VIIRS_{ALT}$, but highlight that these changes (1) are not manifested for all products or all locations, and (2) do not come close to negating the bias between MODIS and VIIRS. The latter is exemplified by the colorscale differences between Figs. 1 and 9, and is contrary to our overarching hypothesis that cross-calibrating the NIRL bands should result in widespread continuity improvements in downstream products. Moreover, noting that Fig. 1 looks almost identical to Fig. S4 (which shows the MPD for the MODIS/$VIIRS_{ALT}$ comparison), it is clear that other sources of uncertainty must be contributing to the discrepancies between MODIS and VIIRS. As the cross-sensor continuity appears to be tied to radiant path geometry, the aerosol models [which include a radiant path geometry component – (Ibrahim et al., 2019)], would be an attractive avenue for assessment. Additionally, while both $L_a(NIR_L)$ and ε are used in aerosol model selection, only the former is substantially changed for a dataset processed with a different $g(NIR_L)$ after SVC. Thus the act of changing g(V862) for these analyses may change the derived L_a spectral magnitude, with downstream impacts on R_{rs} (see Figs. 9 & 10 in Pahlevan et al., 2017a) and C_a. Multiple additional factors are modulated by radiant path geometry, including polarization (Meister et al., 2005; Mobley et al., 2016), Bidirectional Reflectance Distribution Function (Morel and Gentili, 1996, 1991), and instrument calibration corrections for scan angle and time (Sun et al., 2014), and stray light (Barnes et al., 1995). Errors in characterizations and correction of one or multiple of these may thus contribute to remaining cross-sensor biases as noted here.

Despite the directionality implied by setting $g(V862) = 0.97$ in the above analyses, the 3% difference between M'862 and V862 does not actually indicate which of the MODIS or VIIRS $g(NIR_L)$ pre-launch characterizations is more correct. We chose to modify g(V862) as this mimics the format of similar cross calibration exercises (i.e., scaling VIIRS to match MODIS, see Pahlevan et al., 2017b; Sayer et al., 2017). Additionally, as MODIS/A and OLI/Landsat8 appear to be well cross-calibrated with $g(NIR_L) = 1.0$, biases between MODIS/A and VIIRS may reflect errors in the VIIRS calibration (Pahlevan et al., 2017b). Nevertheless, an equally likely potentiality would be $g(V862) = 1.00$ and $g(M869) = 1.03$. Alternatively, as Barnes et al. (Barnes et al., 2020) found an optimal $g(M869) \approx 1.025$, the corresponding g(V862) would be ~0.99–0.995. In this work, we opted to modify gains for only one sensor to allow for simplicity of comparison, and expect that similar trends in cross-sensor continuity would result from any of the other combinations of gains listed above. Nevertheless, these types of studies show potential for improving cross-calibration of standard ocean color products, and therefore should be adopted for operational processing of ocean color data to create more consistent multi-mission products in the past and into the future. Such activites should complement intercalibration against high-quality L_t measurements as derived from planned satellite missions such as CLARREO (Climate Absolute Radiance and Refractivity Observatory) Pathfinder (Goldin et al., 2019).

5. Conclusions

In this work, we assessed the cross-sensor consistency of the NIR_L bands of two mainstream sensors (MODIS/Aqua and VIIRS/SNPP) while weighing techniques commonly used to identify pixel matchups appropriate for satellite cross-calibration. In doing so, we note metrics for spatial homogeneity and relative azimuth are pivotal towards isolating high-quality simultaneous same view (SSV) matchups. Additionally, we found a ~ 3% difference in the pre-launch calibration of the NIR_L bands of the two sensors, with MODIS/A being lower. According to Barnes et al. (Barnes et al., 2020), a change of that magnitude within a single sensor can have substantial impacts on derived ocean color trends in ocean gyres. While global data reprocessed with updated gains to maximize NIR_L cross-calibration consistency showed general improvement in the derived reflectance products, more work is still needed to remediate remaining biases between ocean color sensors.

Declaration of Competing Interest

The authors declare that they have no known competing financial interests or personal relationships that could have appeared to influence the work reported in this paper.

Acknowledgments

This work was supported by funding from the United States National Aeronautics and Space Administration (NASA): NNX16AQ71G (BBB and CH), ROSES 17-TASNPP17-0065 (SWB and BAF), and contract 80GSFC20C0044 (NP). The authors wish to thank NASA for providing the data and processing software used in this work, as well as three anonymous reviewers, whose comments led to substantial improvements in this manuscript.

Appendix A. Supplementary data

Supplementary data to this article can be found online at https://doi.org/10.1016/j.rse.2021.112439.

References

Ahmad, Z., Franz, B.A., McClain, C.R., Kwiatkowska, E.J., Werdell, J., Shettle, E.P., Holben, B.N., 2010. New aerosol models for the retrieval of aerosol optical thickness and normalized water-leaving radiances from the SeaWiFS and MODIS sensors over coastal regions and open oceans. Appl. Opt. https://doi.org/10.1364/AO.49.005545.

Bailey, S.W., Franz, B.A., Werdell, P.J., 2010. Estimation of near-infrared water-leaving reflectance for satellite ocean color data processing. Opt. Express 18, 7521–7527. https://doi.org/10.1364/OE.18.007521.

Barnes, B.B., Hu, C., 2015. Cross-sensor continuity of satellite-derived water clarity in the Gulf of Mexico: insights into temporal aliasing and implications for long-term water clarity assessment. IEEE Trans. Geosci. Remote Sens. 53, 1761–1772. https://doi.org/10.1109/TGRS.2014.2348713.

Barnes, B.B., Hu, C., 2016. Dependence of satellite ocean color data products on viewing angles: a comparison between SeaWiFS, MODIS, and VIIRS. Remote Sens. Environ. 175, 120–129. https://doi.org/10.1016/j.rse.2015.12.048.

Barnes, R.A., Holmes, A.W., Esaias, W.E., 1995. Stray light in the SeaWiFS radiometer. NASA tech memo 104566. In: Hooker, S.B., Firestone, E.R., Acker, J.G. (Eds.), SeaWiFS Technical Report Series, vol. 31.

Barnes, B.B., Cannizzaro, J.P., English, D.C., Hu, C., 2019. Validation of VIIRS and MODIS reflectance data in coastal and oceanic waters: an assessment of methods. Remote Sens. Environ. 220, 110–123. https://doi.org/10.1016/j.rse.2018.10.034.

Barnes, B.B., Hu, C., Bailey, S.W., Franz, B.A., 2020. Sensitivity of satellite ocean color data to system vicarious calibration of the long near infrared band. IEEE Trans. Geosci. Remote Sens. https://doi.org/10.1109/TGRS.2020.3000475.

Bodhaine, B.A., Wood, N.B., Dutton, E.G., Slusser, J.R., 1999. On Rayleigh optical depth calculations. J. Atmos. Ocean. Technol. https://doi.org/10.1175/1520-0426(1999)016<1854:orodc>2.0.co;2.

Bogumil, K., Orphal, J., Homann, T., Voigt, S., Spietz, P., Fleischmann, O.C., Vogel, A., Hartmann, M., Kromminga, H., Bovensmann, H., Frerick, J., Burrows, J.P., 2003. Measurements of molecular absorption spectra with the SCIAMACHY pre-flight model: instrument characterization and reference data for atmospheric remote-sensing in the 230-2380 nm region. J. Photochem. Photobiol. A Chem. https://doi.org/10.1016/S1010-6030(03)00062-5.

Brown, S.W., Flora, S.J., Feinholz, M.E., Yarbrough, M.A., Houlihan, T., Peters, D., Kim, Y.S., Mueller, J.L., Johnson, B.C., Clark, D.K., 2007. The marine optical buoy (MOBY) radiometric calibration and uncertainty budget for ocean color satellite sensor vicarious calibration. In: Sensors, Systems, and Next-Generation Satellites XI. https://doi.org/10.1117/12.737400.

Burkholder, J.B., Talukdar, R.K., 1994. Temperature dependence of the ozone absorption spectrum over the wavelength range 410 to 760 nm. Geophys. Res. Lett. https://doi.org/10.1029/93GL02311.

Chen, J., He, X., Liu, Z., Xu, N., Ma, L., Xing, Q., Hu, X., Pan, D., 2020. An approach to cross-calibrating multi-mission satellite data for the open ocean. Remote Sens. Environ. https://doi.org/10.1016/j.rse.2020.111895.

Djavidnia, S., Mélin, F., Hoepffner, N., 2010. Comparison of global ocean colour data records. Ocean Sci. https://doi.org/10.5194/os-6-61-2010.

Feng, L., Hu, C., 2016. Cloud adjacency effects on top-of-atmosphere radiance and ocean color data products: a statistical assessment. Remote Sens. Environ. 174, 301–313. https://doi.org/10.1016/j.rse.2015.12.020.

Franz, B.A., 2006. gas_trans.c https://doi.org/https://oceancolor.gsfc.nasa.gov/docs/ocssw/gas_trans_8c_source.html.

Franz, B.A., Bailey, S.W., Werdell, P.J., McClain, C.R., 2007. Sensor-independent approach to the vicarious calibration of satellite ocean color radiometry. Appl. Opt. 46, 5068–5082.

Goldin, D., Xiong, X., Shea, Y., Lukashin, C., 2019. CLARREO Pathfinder / VIIRS Intercalibration: Quantifying the Polarization Effects on Reflectance and the Intercalibration Uncertainty. Remote Sensing 11.

Gordon, H.R., 1995. Remote sensing of ocean color: a methodology for dealing with broad spectral bands and significant out-of-band response. Appl. Opt. https://doi.org/10.1364/ao.34.008363.

Gordon, H.R., Clark, D.K., 1981. Clear water radiances for atmospheric correction of coastal zone color scanner imagery. Appl. Opt. 20, 4175–4180. https://doi.org/10.1364/AO.20.004175.

Gordon, H.R., Wang, M., 1994. Retrieval of water-leaving radiance and aerosol optical thickness over the oceans with SeaWiFS: a preliminary algorithm. Appl. Opt. 33, 443–452. https://doi.org/10.1364/AO.33.000443.

Gregg, W.W., Casey, N.W., 2010. Improving the consistency of ocean color data: a step toward climate data records. Geophys. Res. Lett. https://doi.org/10.1029/2009GL041893.

Gregg, W.W., Rousseaux, C.S., 2014. Decadal trends in global pelagic ocean chlorophyll: a new assessment integrating multiple satellites, in situ data, and models. J. Geophys. Res. C Ocean. https://doi.org/10.1002/2014JC010158.

Gregg, W.W., Casey, N.W., McClain, C.R., 2005. Recent trends in global ocean chlorophyll. Geophys. Res. Lett. 32, L03606 https://doi.org/10.1029/2004GL021808.

Henson, S.A., Sarmiento, J.L., Dunne, J.P., Bopp, L., Lima, I., Doney, S.C., John, J., Beaulieu, C., 2010. Detection of anthropogenic climate change in satellite records of ocean chlorophyll and productivity. Biogeosciences. https://doi.org/10.5194/bg-7-621-2010.

Hu, C., Lee, Z., Franz, B., 2012. Chlorophyll a algorithms for oligotrophic oceans: a novel approach based on three-band reflectance difference. J. Geophys. Res. Ocean 117, 1–25. https://doi.org/10.1029/2011JC007395.

Ibrahim, A., Franz, B.A., Ahmad, Z., Bailey, S.W., 2019. Multiband atmospheric correction algorithm for ocean color retrievals. Front. Earth Sci. https://doi.org/10.3389/feart.2019.00116.

Karlsson, K.-G., Johansson, E., 2014. Multi-sensor calibration studies of AVHRR-heritage channel radiances using the simultaneous nadir observation approach. Remote Sens. 6, 1845–1862. https://doi.org/10.3390/rs6031845.

Lee, Z., Shang, S., Hu, C., Lewis, M., Arnone, R., Li, Y., Lubac, B., 2010. Time series of bio-optical properties in a subtropical gyre: implications for the evaluation of interannual trends of biogeochemical properties. J. Geophys. Res. Ocean 115, 1–13. https://doi.org/10.1029/2009JC005865.

Li, R.R., Lewis, M.D., Gould, R.W., Lawson, A., Amin, R., Gallegos, S.C., Ladner, S., 2015. Inter-comparison between VIIRS and MODIS radiances and ocean color data products over the Chesapeake Bay. Remote Sens. 7, 2193–2207. https://doi.org/10.3390/rs70202193.

Meister, G., Kwiatkowska, E.J., Franz, B.A., Patt, F.S., Feldman, G.C., McClain, C.R., 2005. Moderate-resolution imaging spectroradiometer ocean color polarization correction. Appl. Opt. https://doi.org/10.1364/AO.44.005524.

Mélin, F., 2010. Global distribution of the random uncertainty associated with satellite-derived Chl a. IEEE Geosci. Remote Sens. Lett. https://doi.org/10.1109/LGRS.2009.2031825.

Mélin, F., Franz, B.A., 2014. Assessment of satellite ocean colour radiometry and derived geophysical products. In: Experimental Methods in the Physical Sciences. https://doi.org/10.1016/B978-0-12-417011-7.00020-9.

Mélin, F., Sclep, G., Jackson, T., Sathyendranath, S., 2016. Uncertainty estimates of remote sensing reflectance derived from comparison of ocean color satellite data sets. Remote Sens. Environ. https://doi.org/10.1016/j.rse.2016.02.014.

Mobley, C.D., Werdell, J., Franz, B., Ahmad, Z., Bailey, S., 2016. Atmospheric Correction for Satellite Ocean Color Radiometry. Technical Report for Lockheed, NASA/TM-2016-217551, GSFC-E-DAA-TN35509. Greenbelt, MD.

Morel, A., Gentili, B., 1991. Diffuse reflectance of oceanic waters: its dependence on Sun angle as influenced by the molecular scattering contribution. Appl. Opt. https://doi.org/10.1364/ao.30.004427.

Morel, A., Gentili, B., 1996. Diffuse reflectance of oceanic waters. III. Implication of bidirectionality for the remote-sensing problem. Appl. Opt. 35, 4850–4862. https://doi.org/10.1364/AO.35.004850.

Morel, A., Claustre, H., Gentili, B., 2010. The most oligotrophic subtropical zones of the global ocean: similarities and differences in terms of chlorophyll and yellow substance. Biogeosciences 7, 3139–3151. https://doi.org/10.5194/bg-7-3139-2010.

NASA OBPG, n.d. convert_band.c [WWW Document]. URL https://oceancolor.gsfc.nasa.gov/docs/ocssw/convert_band_8c_source.html (accessed 11.11.20).

O'Reilly, J.E., Maritorena, S., Siegel, D.A., O'Brien, M.C., Toole, D., Mitchell, B.G., Kahru, M., Chavez, F.P., Strutton, P., Cota, G.F., Hooker, S.B., McClain, C.R., Carder, K.L., Muller-Karger, F., Harding, L., Magnuson, A., Phinney, D., Moore, G.F., Aiken, J., Arrigo, K.R., Letelier, R., Culver, M., 2000. Ocean color chlorophyll a algorithms for SeaWiFS, OC2 and OC4 : Version 4, NASA tech. memo. 2000–206892. In: Hooker, S.B., Firestone, E.R. (Eds.), SeaWiFS Postlaunch Calibration and Validation Analyses, Part 3, vol. 11. NASA Goddard Space Flight Center, p. 49.

Pahlevan, N., Lee, Z., Wei, J., Schaaf, C.B., Schott, J.R., Berk, A., 2014. On-orbit radiometric characterization of OLI (Landsat-8) for applications in aquatic remote sensing. Remote Sens. Environ. 154, 272–284. https://doi.org/10.1016/j.rse.2014.08.001.

Pahlevan, N., Roger, J.-C., Ahmad, Z., 2017a. Revisiting short-wave-infrared (SWIR) bands for atmospheric correction in coastal waters. Opt. Express. https://doi.org/10.1364/oe.25.006015.

Pahlevan, N., Sarkar, S., Franz, B., 2016. Uncertainties in coastal ocean color products: Impacts of spatial sampling. Remote Sensing of Environment 181, 14–26.

Pahlevan, N., Schott, J.R., Franz, B.A., Zibordi, G., Markham, B., Bailey, S., Schaaf, C.B., Ondrusek, M., Greb, S., Strait, C.M., 2017b. Landsat 8 remote sensing reflectance (Rrs) products: evaluations, intercomparisons, and enhancements. Remote Sens. Environ. https://doi.org/10.1016/j.rse.2016.12.030.

Sayer, A.M., Christina Hsu, N., Bettenhausen, C., Holz, R.E., Lee, J., Quinn, G., Veglio, P., 2017. Cross-calibration of S-NPP VIIRS moderate-resolution reflective solar bands against MODIS aqua over dark water scenes. Atmos. Meas. Tech. https://doi.org/10.5194/amt-10-1425-2017.

Siegel, D.A., Behrenfeld, M.J., Maritorena, S., McClain, C.R., Antoine, D., Bailey, S.W., Bontempi, P.S., Boss, E.S., Dierssen, H.M., Doney, S.C., Eplee, R.E., Evans, R.H., Feldman, G.C., Fields, E., Franz, B.A., Kuring, N.A., Mengelt, C., Nelson, N.B., Patt, F. S., Robinson, W.D., Sarmiento, J.L., Swan, C.M., Werdell, P.J., Westberry, T.K., Wilding, J.G., Yoder, J.A., 2013. Regional to global assessments of phytoplankton dynamics from the SeaWiFS mission. Remote Sens. Environ. https://doi.org/10.1016/j.rse.2013.03.025.

Signorini, S.R., Franz, B.A., McClain, C.R., 2015. Chlorophyll variability in the oligotrophic gyres: mechanisms, seasonality and trends. Front. Mar. Sci. 2, 1–11. https://doi.org/10.3389/fmars.2015.00001.

Sun, J., Xiong, X., Angal, A., Chen, H., Wu, A., Geng, X., 2014. Time-dependent response versus scan angle for MODIS reflective solar bands. IEEE Trans. Geosci. Remote Sens. https://doi.org/10.1109/TGRS.2013.2271448.

Uprety, S., Cao, C., Xiong, X., Blonski, S., Wu, A., Shao, X., 2013. Radiometric intercomparison between suomi-NPP VIIRS and aqua MODIS reflective solar bands using simultaneous nadir overpass in the low latitudes. J. Atmos. Ocean. Technol. 30, 2720–2736. https://doi.org/10.1175/JTECH-D-13-00071.1.

Vantrepotte, V., Mélin, F., 2011. Inter-annual variations in the SeaWiFS global chlorophyll a concentration (1997-2007). Deep. Res. Part I Oceanogr. Res. Pap. https://doi.org/10.1016/j.dsr.2011.02.003.

Wang, M., 2005. A refinement for the Rayleigh radiance computation with variation of the atmospheric pressure. Int. J. Remote Sens. https://doi.org/10.1080/01431160500168793.

Wang, M., Gordon, H.R., 2002. Calibration of ocean color scanners: how much error is acceptable in the near infrared? Remote Sens. Environ. 82, 497–504. https://doi.org/10.1016/S0034-4257(02)00072-X.

Werdell, P.J., Bailey, S.W., 2005. An improved in-situ bio-optical data set for ocean color algorithm development and satellite data product validation. Remote Sens. Environ. 98, 122–140. https://doi.org/10.1016/j.rse.2005.07.001.

Zhang, C., Hu, C., Shang, S., Müller-Karger, F.E., Li, Y., Dai, M., Huang, B., Ning, X., Hong, H., 2006. Bridging between SeaWiFS and MODIS for continuity of chlorophyll-a concentration assessments off Southeastern China. Remote Sens. Environ. https://doi.org/10.1016/j.rse.2006.02.015.

Zibordi, G., Mélin, F., Berthon, J.F., 2012. Intra-annual variations of biases in remote sensing primary ocean color products at a coastal site. Remote Sens. Environ. https://doi.org/10.1016/j.rse.2012.06.016.